

Bimetallic PdAu Nanoframes for Electrochemical H₂O₂ Production in Acids

Xuan Zhao,[▼] Hao Yang,[▼] Jie Xu, Tao Cheng, and Yanguang Li*

Cite This: ACS Materials Lett. 2021, 3, 996–1002



Read Online

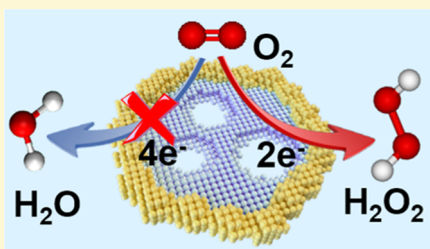
ACCESS |

Metrics & More

Article Recommendations

Supporting Information

ABSTRACT: Electrochemical oxygen reduction reaction via the two-electron pathway to H₂O₂ represents a promising route to enable its on-site, on-demand production for direct consumer use. In particular, running this reaction in acids is practically relevant and scientifically challenging. Herein, we demonstrate that bimetallic PdAu nanoframes can be prepared via stepwise solution growth and etching under well-controlled conditions. The product exhibits a great performance for efficient H₂O₂ production in 0.1 M HClO₄. A positive onset potential and high H₂O₂ yield of >90% are measured, which are considerably improved over pure Au and other Au-based alloys. Theoretical simulations indicate that the incorporation of dilute Pd atoms enhances the adsorption of *OOH as the key intermediate, and thereby promotes the reaction activity and selectivity. Our catalyst can also be used for the electro-Fenton reaction to catalyze the degradation of organic dyes in minutes.



H₂O₂ is an important industrial and household chemical and a potential energy carrier.^{1,2} It is conventionally produced via the energy-intensive anthraquinone oxidation process, which must be performed at centralized facilities and often yields highly concentrated H₂O₂ solution (70 wt %) that is hazardous for transport and storage.^{3,4} Low-concentration H₂O₂ solution (3–9 wt %), on the other hand, is more commonly used at the consumer end for applications such as medical disinfection and wastewater treatment.⁵ This mismatch between the production side and the consumption side motivates people to search for alternative approaches that can enable the on-site, on-demand production of dilute H₂O₂ solution.^{6,7}

Electrochemical H₂O₂ production from oxygen reduction reaction (ORR) has gained increasing attention.^{5,8–12} ORR can proceed via either the four-electron pathway (4e-ORR) or the two-electron pathway (2e-ORR).¹³ To selectively steer the reaction toward the latter for H₂O₂ production requires the use of suitable electrocatalysts that can stabilize the *OOH intermediate and destabilize the *O intermediate.¹⁴ Oxidized carbon materials are demonstrated to have excellent activity and selectivity for 2e-ORR to H₂O₂ under strongly alkaline conditions.^{15–17} Unfortunately, their potentials are very limited since H₂O₂ in alkaline solution has a weaker oxidizing power and quickly decomposes. Electrochemical H₂O₂ production in acids is more scientifically significant and practically relevant.¹⁸ At present, Pt–Hg and Pd–Hg alloys are the state-of-the-art 2e-ORR electrocatalysts in acidic solution,^{14,19} but the incorporation of toxic Hg raises serious health and environmental concerns. Au is a typical 2e-ORR electrocatalyst with

high H₂O₂ selectivity but suffers from low activity in acids, because of its relatively weak *OOH binding.^{20,21} Alloving Au with a secondary metal represents a promising strategy to tailor its electronic structure and thereby electrocatalytic performance. Previous works explored PdAu alloy nanoparticles with different compositions, and reported that the one with 10 at. % Pd exhibited the most enhanced activity without noticeably compromising the selectivity.^{22,23} However, the attainable 2e-ORR performance of Au-based alloys still falls short of people's expectations for practical applications.

In this study, we prepare bimetallic PdAu nanoframes via controlled growth and etching in solution. The product demonstrates much improved onset potential, high selectivity (>90% over a broad potential window) and great stability for 2e-ORR to H₂O₂ in acids—as a result of the stabilized *OOH adsorption evidenced by computational simulations. This catalyst can also be used in the electro-Fenton reaction to facilitate the rapid degradation of organic contaminants in minutes.

Figure 1a schematically illustrates the stepwise synthesis of bimetallic PdAu nanoframes. Pd nanosheets (Pd-ns) were first prepared via the CO-mediated reduction of Pd(II) acetylacetone (Pd(acac)₂) in *N,N*-dimethylformamide (DMF) sol-

Received: April 29, 2021

Accepted: June 10, 2021

Published: June 11, 2021



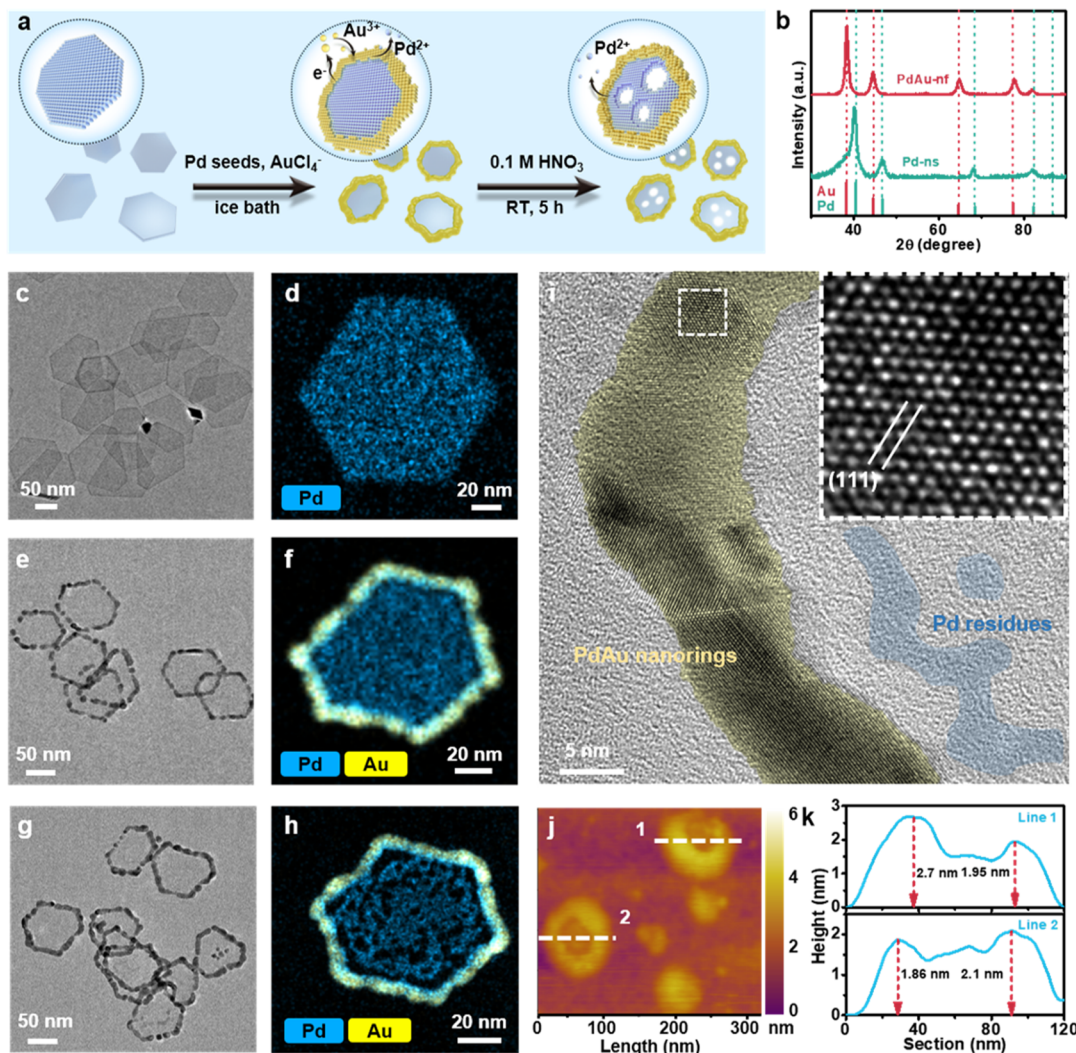


Figure 1. Preparation and characterizations of PdAu-nf: (a) schematic preparation of PdAu-nf via the stepwise growth and etching in solution; (b) XRD patterns of Pd-ns and PdAu-nf; (c) TEM image and (d) EDS mapping of Pd-ns; (e) TEM image and (f) EDS mapping of PdAu@Pd-ns; (g) TEM image and (h) EDS mapping of PdAu-nf; (i) high-resolution TEM images of PdAu-nf showing the alloy ring and attached porous Pd films; (j) AFM image and (k) corresponding height profiles of PdAu-nf.

ution (see experimental details in the Supporting Information).²⁴ Their X-ray diffraction (XRD) pattern exhibits diffraction signals assignable to the standard face-centered cubic (fcc) Pd (Figure 1b). Transmission electron microscopy (TEM) and scanning transmission electron microscopy (STEM) imaging reveals that these nanosheets have a roughly hexagonal shape with the edge length in the range of 60–100 nm and uniform light contrast indicative of small thickness (see Figures 1c and 1d).

For the second step, Pd-ns was redispersed in dilute HAuCl₄ solution cooled in an ice bath. Because of the large difference in the standard reduction potential between Au³⁺/Au (1.498 V versus standard reduction potential or SHE) and Pd²⁺/Pd (0.951 V versus SHE), Pd nanosheets undergo a galvanic replacement reaction with AuCl₄⁻, leading to the deposition of metallic Au nanoparticles preferentially along the nanosheet edges (because of their higher reactivity) and, in the meantime, the gradual Pd dissolution.²⁵ Figure 1e depicts the TEM image of the galvanically replaced product (denoted as PdAu@Pd-ns). Darker nanoparticles are readily identified and coalesce together to form hexagonal rings ~10 nm wide along the nanosheet edges. Compared to the dark rings, the basal planes

of Pd nanosheets become so thin that they are most transparent to the TEM electron beam. Elemental mapping of Au and Pd using energy-dispersive spectroscopy (EDS) attests that Pd is distributed throughout the nanosheet whereas the Au signal is concentrated at the edges (Figure 1f). The partial overlap in the spatial distribution of Pd and Au evidence that the ring is mainly composed of their bimetallic alloy instead of pure Au—as a result of the interdiffusion between Au and Pd during the galvanic replacement reaction.²⁶ By controlling the added amount of HAuCl₄, the ring thickness can be tuned from a few nanometers to >20 nm, as shown in Figure S1 in the Supporting Information.

Since we are unable to completely dissolve metallic Pd (which is a typical 4e-ORR electrocatalyst) via galvanic replacement, PdAu@Pd-ns was further chemically etched in dilute HNO₃ to selectively remove Pd.^{27,28} One key factor in this step is the etching time: insufficient etching leaves considerable Pd residues while overetching compromises the structural integrity. The optimum etching time is determined to be ~5 h, giving rise to PdAu nanoframes (PdAu-nf) as the final product. XRD pattern of PdAu-nf shows a set of diffraction peaks noticeably displaced toward the lower angle

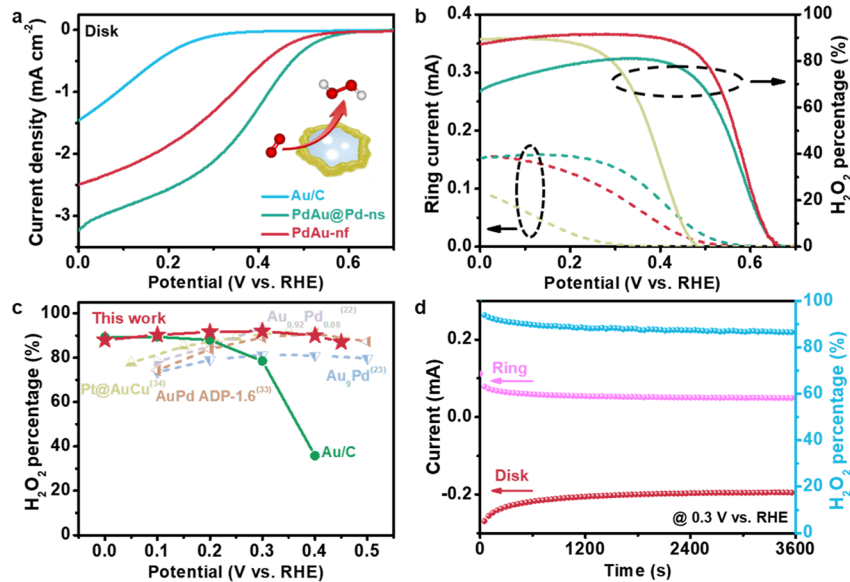


Figure 2. Electrochemical performance of PdAu-nf for 2e-ORR to H₂O₂. (a) Disk polarization curves of Au/C, PdAu@Pd-ns, and PdAu-nf at 1600 rpm in O₂-saturated 0.1 M HClO₄; (b) corresponding ring current and H₂O₂ percentage of Au/C, PdAu@Pd-ns, and PdAu-nf; (c) comparison of the potential-dependent H₂O₂ percentage of our PdAu-nf with relevant literature results; (d) change of the disk current, ring current, and H₂O₂ percentage with time when biased under 0.3 V at 1600 rpm in O₂-saturated 0.1 M HClO₄.

direction, relative to those of Pd-ns and close to those of pure Au (Figure 1b), indicating the formation of a PdAu alloy enriched with Au. Inductively coupled plasma–mass spectrometry (ICP-MS) analysis indicates that the product is composed of ~91 at. % Au and ~9 at. % Pd. When examined under TEM and STEM, PdAu-nf is shown to preserve the overall hexagonal shape (Figure 1g). However, the Pd interior becomes corroded, leaving porous thin films attached onto the rigid PdAu framework, as evidently illustrated from the EDS mapping (Figure 1h). A high-resolution TEM image reveals obvious lattice fringes assignable to the (111) plane of the alloy as well as the grain boundary from the coalescence of neighboring nanoparticles (Figure 1i). Moreover, we performed atomic force microscopy (AFM) analysis of PdAu-nf. Even though it does not have sufficient lateral resolution to unveil the spatial feature of nanoframes (Figure 1j), the height profiles disclose that each nanoframe is 2~3 nm thick (Figure 1k). Pd 3d X-ray photoelectron spectroscopy (XPS) of PdAu-nf exhibits a doublet positively shifted by 0.7–0.8 eV, relative to that of Pd-ns (Figure S2 in the Supporting Information). Its Au 4f doublet is negatively shifted by ~0.1 eV, relative to that of pure Au. These results suggest the charge transfer from Pd to Au upon alloying, in agreement with previous observations.^{29,30} The different degrees of shift reflect that the electronic state of minor Pd atoms is more effectively modulated by surrounding Au atoms in PdAu-nf.

We next examined the electrocatalytic performance of PdAu-nf for 2e-ORR to H₂O₂ in 0.1 M HClO₄. Catalyst powders were blended with carbon black and Nafion binder, and dropcast onto the glassy carbon disk of rotating ring disk electrodes (RRDEs) (see experimental details in Supporting Information). Produced H₂O₂ was electrochemically detected and analyzed by the Pt ring. No ORR response is measured when the electrolyte is saturated with N₂ (Figure S3). In the presence of O₂, Pd-ns exhibits a positive onset potential of ~0.9 V (versus reversible hydrogen electrode or RHE, the same hereinafter) and low H₂O₂ percentage (<20%), in line with the predominant 4e-ORR selectivity of pure Pd (Figure

S4).^{31,32} 20 wt % Au/C prepared via a standard method has great H₂O₂ yield (~90%), but its activity is low with a poor onset potential of ~0.35 V — also consistent with literature results (Figure 2a,b).^{22,23} Alloying Au and Pd can inherit and integrate the advantages of both. PdAu@Pd-ns directly from the galvanic replacement reaction has a positive onset potential of 0.6 V (close to the theoretical value of 0.7 V) as well as decent H₂O₂ percentage of 70~80%. Further chemical etching to PdAu-nf slightly sacrifices the onset potential (0.56 V) and cathodic current density (1.9 mA cm⁻² at 0.2 V), but enhances the H₂O₂ percentage to >90% over a wide potential window. Such a combination of positive onset potential and high H₂O₂ selectivity is superior to other Au-based alloys available in literature in our best knowledge (Figure 2c).^{22,23,33,34} Moreover, the effect of catalyst loading on the 2e-ORR performance is explored, and the results are summarized in Figure S5 in the Supporting Information.

H₂O₂ selectivity is collectively determined by the H₂O₂ production rate and degradation rate. A good electrocatalyst can enable fast H₂O₂ production and at the same time suppress its degradation via O–O bond dissociation. In order to understand the selectivity trend in Figure 2b, we evaluated the H₂O₂ degradation activities of four different samples in N₂-saturated 0.1 M HClO₄ solution containing 10 mM H₂O₂ (Figure S6 in the Supporting Information).³⁵ Pd-ns exhibits pronounced cathodic current density up to ~17 mA cm⁻², while Au/C has zero activity over the entire potential regime. Bimetallic PdAu alloys demonstrate H₂O₂ reduction activities between pure Pd and Au. The cathodic current density is measured to be 4 mA cm⁻² and 1.8 mA cm⁻² at 0.2 V for PdAu@Pd-ns and PdAu-nf, respectively. This leads us to conclude that alloying Au with an increasing amount of Pd promotes the ORR activity but compromises the H₂O₂ selectivity by accelerating its degradation. Only at a particular composition (~10 at. % Pd) can the optimum performance be achieved with balanced activity and selectivity.

Furthermore, we assessed the operation stability of PdAu-nf. When the working electrode was biased at 0.3 V, both the disk

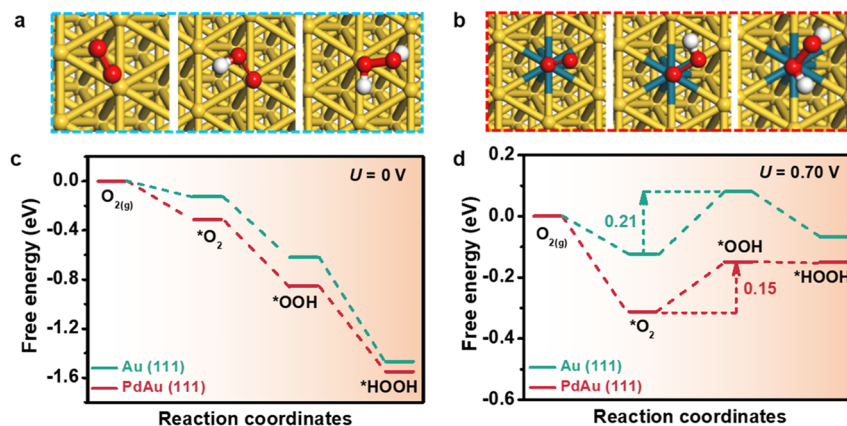


Figure 3. DFT simulations of the 2e-ORR pathway on Au(111) and PdAu(111): (a,b) optimized adsorption configuration of $^*\text{O}_2$, $^*\text{OOH}$, and $^*\text{HOOH}$ intermediates on Au(111) (panel (a)) and PdAu(111) (panel (b)); (c,d) free-energy changes during 2e-ORR to H_2O_2 on Au(111) and PdAu(111) under $U = 0 \text{ V}$ (panel (c)) and $U = 0.70 \text{ V}$ (panel (d)).

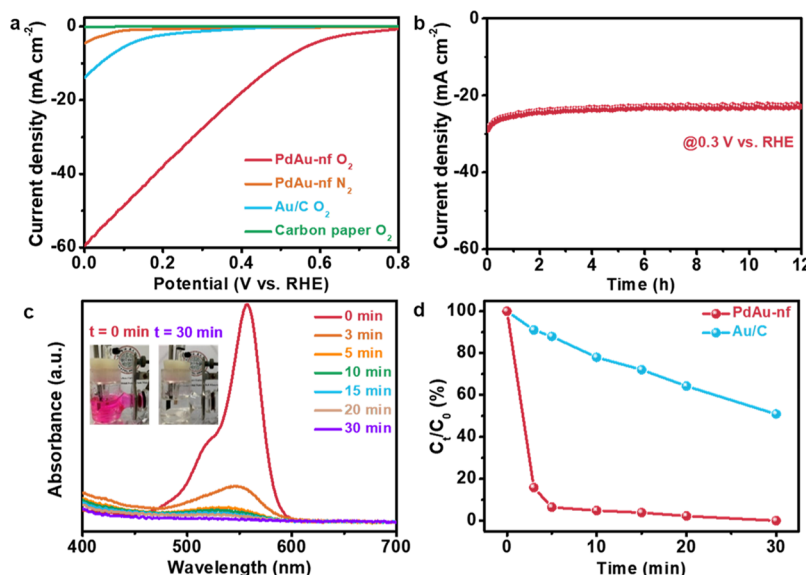


Figure 4. Electro-Fenton application of PdAu-nf. (a) Polarization curves of PdAu-nf and Au/C on the carbon fiber paper electrode in N_2 - or O_2 -saturated $0.5 \text{ M Na}_2\text{SO}_4$ solution ($\text{pH} = 2$); (b) chronoamperometric ($i-t$) curve of PdAu-nf at 0.3 V for 12 h ; (c) UV-vis absorption spectrum of the RhB solution after the electro-Fenton reaction at 0.3 V for different times as indicated, inset shows the solution color change after 30 min reaction; (d) decay of the RhB concentration over time during the electro-Fenton reaction at 0.3 V catalyzed by PdAu-nf or Au/C.

current and ring current experience a quick initial decrease and then remain almost constant (Figure 2d). The H_2O_2 yield remains $\sim 87\%$ after 1 h. In addition, accelerated durability test was conducted by rapidly cycling the catalyst between 0 and 0.4 V in O_2 -saturated 0.1 M HClO_4 for several cycles, and then recording its polarization curves. Compared to the original one, the polarization curves after 2500, 5000, and 10 000 cycles are slightly displaced toward the negative direction, but the activity loss is limited and mostly occurs in the first 5000 cycles (see Figure S7 in the Supporting Information). The ring current and corresponding H_2O_2 yield are also subjected to minor decreases with cycling. TEM analysis of spent PdAu-nf recovered after the stability test shows that most nanoframes retain their structure and composition although individual alloy nanoparticles are sometime observed (see Figure S8 in the Supporting Information). The aforementioned studies support the decent operation stability of our bimetallic nanoframes.

Future improvements can be made by fine-tuning their nanostructure and composition.

To gain insights into the atomic origin of the enhanced activity and selectivity observed for bimetallic PdAu nanoframes, density functional theory (DFT) calculations were performed to simulate the 2e-ORR reaction pathway. Pure Au was modeled using the $3 \times 3 \times 4$ Au(111) surface slab, since it is the most stable facet of fcc Au. PdAu alloy was modeled by replacing one surface Au atom in $3 \times 3 \times 4$ Au(111) with one Pd atom, resulting in the Au/Pd atomic ratio of 8 close to the actual chemical composition of PdAu-nf (Figure S9 in the Supporting Information). We do not consider the influence of porous Pd films in PdAu-nf in order to make our computational analysis more straightforward. It is generally believed that 2e-ORR proceeds via the reaction $^*\text{O}_2 \rightarrow ^*\text{OOH} \rightarrow ^*\text{HOOH}$ with the second step being the rate-determining step and the $^*\text{OOH}$ adsorption energy as the activity descriptor.¹⁴ In addition to this pathway, the O–O bond would be cleaved if

*O is stabilized on the catalyst surface, and eventually leads to the formation of water as the 4e-ORR product.¹³ Here, our calculations show that the formation energy of *O is -1.27 , $+0.72$, and $+1.05$ eV on Pd(111), PdAu(111), and Au(111), respectively, at $U = 0.7$ V, indicating that 4e-ORR is thermodynamically favorable on Pd whereas 2e-ORR is more competitive on PdAu(111) and Au(111) (see Figure S10 in the Supporting Information).

Figures 3a and 3b depicts the most stable adsorption configuration of 2e-ORR intermediates on Au(111) and PdAu(111). The reaction energetics under $U = 0$ V (the standard condition) and $U = 0.7$ V (the equilibrium potential for H_2O_2 production) is illustrated in Figures 3c and 3d. Most remarkably, *OOH is considerably stabilized on PdAu(111) (-0.55 eV at $U = 0$), relative to Au(111) (-0.49 eV at $U = 0$). The free-energy difference for the *OOH formation becomes evident under $U = 0.7$ V, and is lowered from $+0.21$ eV on Au(111) to $+0.15$ eV on PdAu(111). The incorporation of an isolated Pd atom in PdAu(111) stabilizes the adsorption of *OOH through the direct Pd–O bonding and thereby promotes the 2e-ORR activity. For PdAu alloys with higher Pd contents, Pd atoms start to form dimers and even multimers on the catalyst surface, which would instead facilitate O–O dissociation and compromise the H_2O_2 selectivity. The aforementioned computational results fully support and rationalize our experimental observations.

At last, we investigated the potential application of our bimetallic nanoframes for the electro-Fenton reaction, where electrochemically generated H_2O_2 reacts with Fe^{2+} to produce hydroxyl radicals for the on-site degradation of organic contaminants.^{36,37} We used Teflon-treated carbon fiber paper as the gas diffusion electrode instead of RRDE in order to promote O_2 diffusion, and Rhodamine B (RhB) as the model organic contaminant and color indicator (see experimental details in the Supporting Information). Figure 4a depicts the polarization curves of samples in N_2 or O_2 -saturated 0.5 M acidic Na_2SO_4 (pH adjusted to 2 using dilute H_2SO_4). The carbon fiber paper alone has a negligible ORR activity. Au/C exhibits a poor onset potential of ~ 0.3 V and delivers current density of 13.6 mA cm^{-2} at 0 V in the presence of O_2 . By stark contrast, PdAu-nf is able to sustain a significantly larger cathodic current density when the O_2 diffusion limitation is alleviated, reaching $\sim 59 \text{ mA cm}^{-2}$ at 0 V. This large current density does not sacrifice the catalyst stability: it retains a stable current density of $\sim 23 \text{ mA cm}^{-2}$ when biased at 0.3 V for 12 h, as shown in Figure 4b. When applied to the electro-Fenton reaction, PdAu-nf enables the rapid degradation of RhB in minutes from its 20 mg L^{-1} solution (in 0.5 M acidic Na_2SO_4 for the best performance). The original solution has a pink color and a prominent absorption peak at 557 nm from its ultraviolet-visible (UV-vis) spectrum that are characteristic to RhB (Figure 4c). Upon the application of a working potential of 0.3 V, the solution color quickly fades and becomes colorless within 30 min. UV-vis analysis of the catholyte allows us to quantify the degradation rate and indicates that $\sim 90\%$ of RhB is consumed within the first 5 min (Figure 4d). Control experiment with Au/C reveals that the standard material is much less efficient. More than 50% RhB remains in the catholyte even after 30 min of reaction.

In summary, bimetallic PdAu nanoframes were prepared via stepwise solution growth and etching. The best product consisted of alloy rings of ~ 10 nm wide attached with porous Pd films, and it was analyzed to have an Au/Pd atomic ratio of

~ 9 . In O_2 -saturated 0.1 M HClO_4 , PdAu-nf enabled efficient 2e-ORR to H_2O_2 and exhibited a balanced activity and selectivity. It was measured to have positive onset potential (~ 0.56 V versus RHE), high H_2O_2 yield ($>90\%$ over a broad potential window) and decent stability—markedly improved over pure Au and superior to other Au-based alloys. DFT calculations indicated that the great performance was originated from the stabilized *OOH adsorption via direct Pd–O bonding with isolated Pd atoms in the alloy. In addition, our product was applied for the electro-Fenton reaction, and catalyzed the rapid degradation of RhB in minutes. Our study demonstrates that via proper alloying and nanostructuring, the great potential of Au-based materials could be unlocked for the electrochemical H_2O_2 production in acids.

ASSOCIATED CONTENT

SI Supporting Information

The Supporting Information is available free of charge at <https://pubs.acs.org/doi/10.1021/acsmaterialslett.1c00263>.

Experimental details, TEM images, XPS spectra, electrochemical analysis and DFT simulation (PDF)

AUTHOR INFORMATION

Corresponding Author

Yanguang Li – Institute of Functional Nano & Soft Materials (FUNSOM), Jiangsu Key Laboratory for Carbon-Based Functional Materials and Devices, Soochow University, Suzhou 215123, China; Macao Institute of Materials Science and Engineering, Macau University of Science and Technology, Taipa 999078, Macau SAR, China;
✉ orcid.org/0000-0003-0506-0451; Email: yanguang@suda.edu.cn

Authors

Xuan Zhao – Institute of Functional Nano & Soft Materials (FUNSOM), Jiangsu Key Laboratory for Carbon-Based Functional Materials and Devices, Soochow University, Suzhou 215123, China

Hao Yang – Institute of Functional Nano & Soft Materials (FUNSOM), Jiangsu Key Laboratory for Carbon-Based Functional Materials and Devices, Soochow University, Suzhou 215123, China; ✉ orcid.org/0000-0002-8241-6231

Jie Xu – Institute of Functional Nano & Soft Materials (FUNSOM), Jiangsu Key Laboratory for Carbon-Based Functional Materials and Devices, Soochow University, Suzhou 215123, China

Tao Cheng – Institute of Functional Nano & Soft Materials (FUNSOM), Jiangsu Key Laboratory for Carbon-Based Functional Materials and Devices, Soochow University, Suzhou 215123, China; ✉ orcid.org/0000-0003-4830-177X

Complete contact information is available at:
<https://pubs.acs.org/10.1021/acsmaterialslett.1c00263>

Author Contributions

These authors contributed equally.

Notes

The authors declare no competing financial interest.

■ ACKNOWLEDGMENTS

We acknowledge the support from the Ministry of Science and Technology of China (No. 2017YFA0204800), the National Natural Science Foundation of China (Nos. U2002213 and 21903058), the Natural Science Foundation of Jiangsu Province (No. BK20190810), the China Postdoctoral Science Foundation (No. 2019M660128), the Collaborative Innovation Center of Suzhou Nano Science and Technology, the 111 Project, and Joint International Research Laboratory of Carbon-Based Functional Materials and Devices.

■ REFERENCES

- (1) Fukuzumi, S.; Yamada, Y.; Karlin, K. D. Hydrogen peroxide as a sustainable energy carrier: Electrocatalytic production of hydrogen peroxide and the fuel cell. *Electrochim. Acta* **2012**, *82*, 493–511.
- (2) Ciriminna, R.; Albanese, L.; Meneguzzo, F.; Pagliaro, M. Hydrogen peroxide: A key chemical for today's sustainable development. *ChemSusChem* **2016**, *9*, 3374–3381.
- (3) Samanta, C. Direct synthesis of hydrogen peroxide from hydrogen and oxygen: An overview of recent developments in the process. *Appl. Catal., A* **2008**, *350*, 133–149.
- (4) Campos-Martin, J. M.; Blanco-Brieva, G.; Fierro, J. L. G. Hydrogen peroxide synthesis: An outlook beyond the anthraquinone process. *Angew. Chem., Int. Ed.* **2006**, *45*, 6962–6984.
- (5) Yang, S.; Verdaguera-Casadevall, A.; Arnarson, L.; Silvioli, L.; Colic, V.; Frydendal, R.; Rossmeisl, J.; Chorkendorff, I.; Stephens, I. E. L. Toward the decentralized electrochemical production of H₂O₂: A Focus on the catalysis. *ACS Catal.* **2018**, *8*, 4064–4081.
- (6) Xia, C.; Xia, Y.; Zhu, P.; Fan, L.; Wang, H. Direct electrosynthesis of pure aqueous H₂O₂ solutions up to 20% by weight using a solid electrolyte. *Science* **2019**, *366*, 226–231.
- (7) Jiang, K.; Back, S.; Akey, A. J.; Xia, C.; Hu, Y. F.; Liang, W. T.; Schaak, D.; Stavitski, E.; Norskov, J. K.; Siahrostami, S.; Wang, H. T. Highly selective oxygen reduction to hydrogen peroxide on transition metal single atom coordination. *Nat. Commun.* **2019**, *10*, 3997.
- (8) Jiang, Y. Y.; Ni, P. J.; Chen, C. X.; Lu, Y. Z.; Yang, P.; Kong, B.; Fisher, A.; Wang, X. Selective electrochemical H₂O₂ production through two-electron oxygen electrochemistry. *Adv. Energy Mater.* **2018**, *8*, 1801909.
- (9) Jiang, K.; Zhao, J. J.; Wang, H. T. Catalyst design for electrochemical oxygen reduction toward hydrogen peroxide. *Adv. Funct. Mater.* **2020**, *30*, 2003321.
- (10) Zhang, J. Y.; Zhang, H. C.; Cheng, M. E.; Lu, Q. Tailoring the electrochemical production of H₂O₂: Strategies for the rational design of high-performance electrocatalysts. *Small* **2020**, *16*, 1902845.
- (11) Perry, S. C.; Pangotra, D.; Vieira, L.; Csepei, L. I.; Sieber, V.; Wang, L.; Ponce de Leon, C.; Walsh, F. C. Electrochemical synthesis of hydrogen peroxide from water and oxygen. *Nat. Rev. Chem.* **2019**, *3*, 442–458.
- (12) Zhao, X.; Wang, Y.; Da, Y. L.; Wang, X. X.; Wang, T. T.; Xu, M. Q.; He, X. Y.; Zhou, W.; Li, Y. F.; Coleman, J. N.; Li, Y. G. Selective electrochemical production of hydrogen peroxide at zigzag edges of exfoliated molybdenum telluride nanoflakes. *Natl. Sci. Rev.* **2020**, *7*, 1360–1366.
- (13) Kulkarni, A.; Siahrostami, S.; Patel, A.; Norskov, J. K. Understanding catalytic activity trends in the oxygen reduction reaction. *Chem. Rev.* **2018**, *118*, 2302–2312.
- (14) Siahrostami, S.; Verdaguera-Casadevall, A.; Karamad, M.; Deiana, D.; Malacrida, P.; Wickman, B.; Escudero-Escribano, M.; Paoli, E. A.; Frydendal, R.; Hansen, T. W.; Chorkendorff, I.; Stephens, I. E. L.; Rossmeisl, J. Enabling direct H₂O₂ production through rational electrocatalyst design. *Nat. Mater.* **2013**, *12*, 1137–1143.
- (15) Lu, Z. Y.; Chen, G. X.; Siahrostami, S.; Chen, Z. H.; Liu, K.; Xie, J.; Liao, L.; Wu, T.; Lin, D. C.; Liu, Y. Y.; Jaramillo, T. F.; Norskov, J. K.; Cui, Y. High-efficiency oxygen reduction to hydrogen peroxide catalysed by oxidized carbon materials. *Nat. Catal.* **2018**, *1*, 156–162.
- (16) Kim, H. W.; Ross, M. B.; Kornienko, N.; Zhang, L.; Guo, J. H.; Yang, P. D.; McCloskey, B. D. Efficient hydrogen peroxide generation using reduced graphene oxide-based oxygen reduction electrocatalysts. *Nat. Catal.* **2018**, *1*, 282–290.
- (17) Liu, Y. M.; Quan, X.; Fan, X. F.; Wang, H.; Chen, S. High-yield electrosynthesis of hydrogen peroxide from oxygen reduction by hierarchically porous carbon. *Angew. Chem., Int. Ed.* **2015**, *54*, 6837–6841.
- (18) Gao, J. J.; Yang, H. B.; Huang, X.; Hung, S. F.; Cai, W. Z.; Jia, C. M.; Miao, S.; Chen, H. M.; Yang, X. F.; Huang, Y. Q.; Zhang, T.; Liu, B. Enabling direct H₂O₂ production in acidic media through rational design of transition metal single atom catalyst. *Chem.* **2020**, *6*, 658–674.
- (19) Verdaguera-Casadevall, A.; Deiana, D.; Karamad, M.; Siahrostami, S.; Malacrida, P.; Hansen, T. W.; Rossmeisl, J.; Chorkendorff, I.; Stephens, I. E. L. Trends in the electrochemical synthesis of H₂O₂: Enhancing activity and selectivity by electrocatalytic site engineering. *Nano Lett.* **2014**, *14*, 1603–1608.
- (20) Yang, Y.; Dai, C. Q.; Fisher, A.; Shen, Y. C.; Cheng, D. J. A full understanding of oxygen reduction reaction mechanism on Au (111) surface. *J. Phys.: Condens. Matter* **2017**, *29*, 365201.
- (21) Vazquez-Huerta, G.; Ramos-Sanchez, G.; Rodriguez-Castellanos, A.; Meza-Calderon, D.; Antano-Lopez, R.; Solorza-Feria, O. Electrochemical analysis of the kinetics and mechanism of the oxygen reduction reaction on Au nanoparticles. *J. Electroanal. Chem.* **2010**, *645*, 35–40.
- (22) Pizzutilo, E.; Kasián, O.; Choi, C. H.; Cherevko, S.; Hutchings, G. J.; Mayrhofer, K. J. J.; Freakley, S. J. Electrocatalytic synthesis of hydrogen peroxide on Au-Pd nanoparticles: From fundamentals to continuous production. *Chem. Phys. Lett.* **2017**, *683*, 436–442.
- (23) Jirkovský, J. S.; Panas, I.; Ahlberg, E.; Halasa, M.; Romani, S.; Schiffrin, D. J. Single atom hot-spots at Au-Pd nanoalloys for electrocatalytic H₂O₂ production. *J. Am. Chem. Soc.* **2011**, *133*, 19432–19441.
- (24) Huang, X. Q.; Tang, S. H.; Mu, X. L.; Dai, Y.; Chen, G. X.; Zhou, Z. Y.; Ruan, F. X.; Yang, Z. L.; Zheng, N. F. Freestanding palladium nanosheets with plasmonic and catalytic properties. *Nat. Nanotechnol.* **2011**, *6*, 28–32.
- (25) Zhao, M.; Wang, X.; Yang, X.; Gilroy, K. D.; Qin, D.; Xia, Y. N. Hollow metal nanocrystals with ultrathin, porous walls and well-controlled surface structures. *Adv. Mater.* **2018**, *30*, 1801956.
- (26) Rezaei, B.; Havakeshian, E.; Ensafi, A. A. Electrocatalytic activity of bimetallic Pd-Au nanostructure supported on nanoporous stainless steel surface using galvanic replacement reaction toward the glycerol oxidation in alkaline media. *J. Electroanal. Chem.* **2016**, *782*, 108–116.
- (27) Wang, W. X.; Yan, Y. C.; Zhou, N.; Zhang, H.; Li, D. S.; Yang, D. R. Seed-mediated growth of Au nanorings with size control on Pd ultrathin nanosheets and their tunable surface plasmonic properties. *Nanoscale* **2016**, *8*, 3704–3710.
- (28) Zhang, H.; Jin, M. S.; Xia, Y. N. Noble-metal nanocrystals with concave surfaces: Synthesis and applications. *Angew. Chem., Int. Ed.* **2012**, *51*, 7656–7673.
- (29) Enache, D. I.; Edwards, J. K.; Landon, P.; Solsona-Espriu, B.; Carley, A. F.; Herzing, A. A.; Watanabe, M.; Kiely, C. J.; Knight, D. W.; Hutchings, G. J. Solvent-free oxidation of primary alcohols to aldehydes using Au-Pd/TiO₂ catalysts. *Science* **2006**, *311*, 362–365.
- (30) Yuan, X. T.; Zhang, L.; Li, L. L.; Dong, H.; Chen, S.; Zhu, W. J.; Hu, C. L.; Deng, W. Y.; Zhao, Z. J.; Gong, J. L. Ultrathin Pd-Au shells with controllable alloying degree on Pd nanocubes toward carbon dioxide reduction. *J. Am. Chem. Soc.* **2019**, *141*, 4791–4794.
- (31) Xiao, L.; Zhuang, L.; Liu, Y.; Lu, J. T.; Abruna, H. D. Activating Pd by morphology tailoring for oxygen reduction. *J. Am. Chem. Soc.* **2009**, *131*, 602–608.
- (32) Xu, H.; Shang, H. Y.; Wang, C.; Du, Y. K. Recent progress of ultrathin 2D Pd-based nanomaterials for fuel cell electrocatalysis. *Small* **2021**, *17*, 2005092.
- (33) Pizzutilo, E.; Freakley, S. J.; Cherevko, S.; Venkatesan, S.; Hutchings, G. J.; Liebscher, C. H.; Dehm, G.; Mayrhofer, K. J. J.

Gold-palladium bimetallic catalyst stability: Consequences for hydrogen peroxide selectivity. *ACS Catal.* **2017**, *7*, 5699–5705.

(34) Shi, Q. R.; Zhu, W. L.; Zhong, H.; Zhu, C. Z.; Tian, H. Y.; Li, J. C.; Xu, M. J.; Su, D.; Li, X.; Liu, D.; Xu, B. Z.; Beckman, S. P.; Du, D.; Lin, Y. H. Highly dispersed platinum atoms on the surface of AuCu metallic aerogels for enabling H_2O_2 production. *ACS Appl. Energy Mater.* **2019**, *2*, 7722–7727.

(35) Tang, C.; Jiao, Y.; Shi, B. Y.; Liu, J. N.; Xie, Z. H.; Chen, X.; Zhang, Q.; Qiao, S. Z. Coordination tunes selectivity: Two-electron oxygen reduction on high-loading molybdenum single-atom catalysts. *Angew. Chem., Int. Ed.* **2020**, *59*, 9171–9176.

(36) Brillas, E.; Sires, I.; Oturan, M. A. Electro-Fenton process and related electrochemical technologies based on Fenton's reaction chemistry. *Chem. Rev.* **2009**, *109*, 6570–6631.

(37) Nidheesh, P. V.; Gandhimathi, R. Trends in electro-Fenton process for water and wastewater treatment: An overview. *Desalination* **2012**, *299*, 1–15.